Supporting Information 2

Comparative Structural Analysis of PtCo and PtNi Bimetallic Clusters: A Systematic Study Using MCDE Algorithm

Contents

Section S1: Algorithm Performance Validation

Figure S1. Algorithm performance for $Pt_{27}Co_{28}$ system

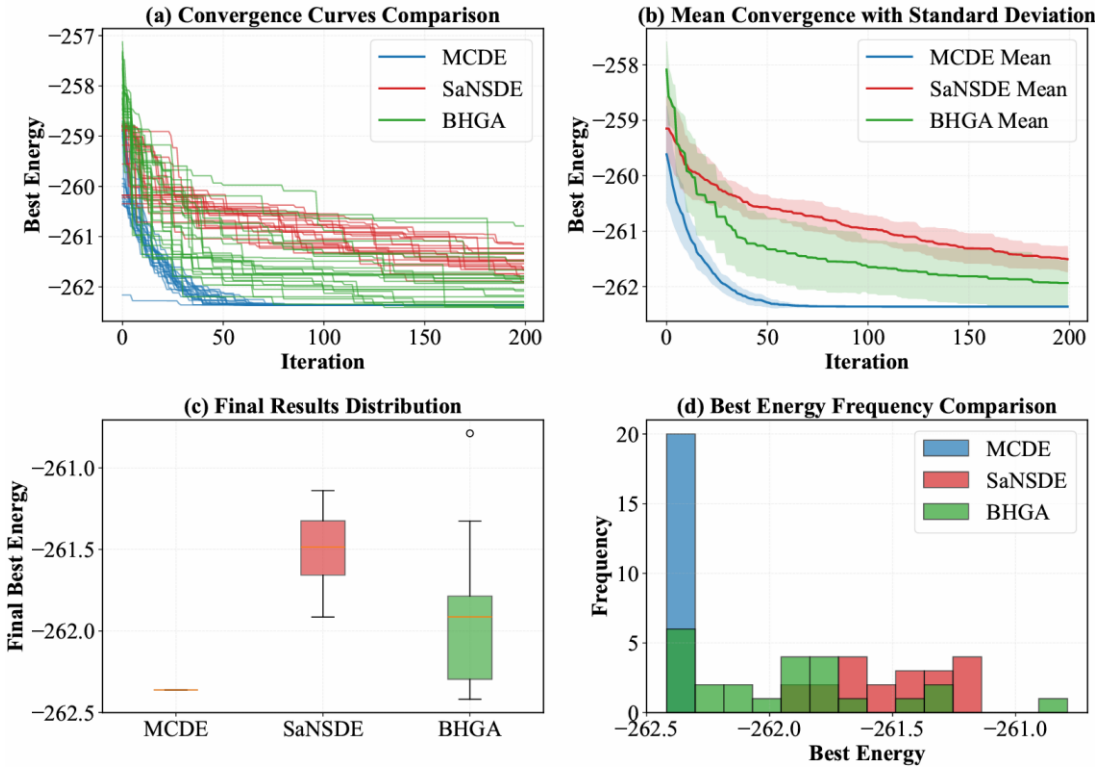

Figure S1. Algorithm performance comparison for $Pt_{27}Co_{28}$ cluster optimization based on 20 independent runs. (a) Convergence trajectories for individual runs; (b) Average convergence curves with standard deviation bands; (c) Box plots showing distribution of final energies; (d) Histogram of best energy values achieved.

Table S1. Algorithm Performance Metrics for $Pt_{27}Co_{28}$ Cluster Structure Optimization.

Algorithm	Mean	Std	Min	Max
MCDE	-262.361698	0.000000	-262.361698	-262.361698
SaNSDE	-261.505059	0.227068	-261.914646	-261.139615
BHGA	-261.935477	0.402275	-262.361698	-260.788247

For the $Pt_{27}Co_{28}$ system, MCDE demonstrates superior performance with perfect consistency and identifies the same optimal structure (-262.361698 eV) across all runs. In comparison, SaNSDE shows a mean energy of -261.505059 eV with a standard deviation of 0.227068 eV, while BHGA achieves a mean of -261.935477 eV with a standard deviation of 0.402275 eV. MCDE obtains energies approximately 0.86 eV and 0.43 eV lower than SaNSDE and BHGA respectively, with significantly enhanced reliability as evidenced by its zero standard deviation compared to the substantial variations observed in SaNSDE and BHGA.

Section S2: DFT Validation of Gupta Potential

To validate the applicability of the Gupta potential parameters in our systems, we have performed DFT single-point energy calculations on representative structures. We selected two structures each from $Pt_{19}Ni_{19}$ and $Pt_{19}Co_{19}$ clusters for comparison. The results show that for the $Pt_{19}Ni_{19}$ system, the Gupta potential yields energies of -164.765 eV and -164.506 eV (energy difference 0.258 eV) for the two structures, while the corresponding DFT calculations give -241126.458 eV and -241126.138 eV (energy difference 0.320 eV). For the $Pt_{19}Co_{19}$ system, the Gupta potential predicts energies of -177.309 eV and -177.093 eV (energy difference 0.217 eV), with DFT results of -290508.227 eV and -290507.060 eV (energy difference 1.167 eV). These data reveal significant quantitative deviations in the relative energy differences between the two methods, with approximately 5-fold difference observed in the $Pt_{19}Co_{19}$ system. This stems from fundamental differences in their computational frameworks: the Gupta potential, as a semi-empirical approach, calculates cohesive energy through parameterized pairwise and many-body interactions, while DFT, as a first-principles method, computes total electronic energy based on quantum mechanics including electron correlation and exchange effects. It should be noted that in the current validation, both methods happen to yield consistent stability rankings for the tested structures; however, due to the fundamental differences in computational principles, the Gupta potential and DFT may produce different stability orderings in some cases. Such inconsistencies are expected and do not indicate failure of the potential function, but rather reflect the inherent limitations of semi-empirical methods.

Table S2. Comparison of Gupta Potential and DFT Energies for Representative Structures.

System	Structure	Gupta (eV)	DFT (eV)	ΔE(Gupta)	ΔE(DFT)
$Pt_{19}Ni_{19}$	Str-1	-164.765	-241126.458	**0.000**	**0.000**
$Pt_{19}Ni_{19}$	Str-2	-164.506	-241126.138	**+0.258**	**+0.320**
$Pt_{19}Co_{19}$	Str-1	-177.309	-290508.227	**0.000**	**0.000**
$Pt_{19}Co_{19}$	Str-2	-177.093	-290507.060	**+0.217**	**+1.167**

In this study, the primary role of the Gupta potential is to serve as an efficient pre-screening tool for rapidly identifying energetically favorable candidate structures from vast configuration spaces containing thousands of structures, which dramatically reduces computational costs and enables systematic exploration. Structures identified as low-energy candidates by the Gupta potential are subsequently validated using DFT calculations to ensure the reliability of final conclusions. This hierarchical "potential screening + first-principles validation" strategy achieves a reasonable balance between computational efficiency and result accuracy. The present validation demonstrates that, while the Gupta potential cannot provide quantitative accuracy comparable to DFT, it offers practical value for rapidly assessing the relative stability of numerous structures. This methodology has been widely adopted in research areas such as nanoclusters where exploration of complex potential energy surfaces is required.

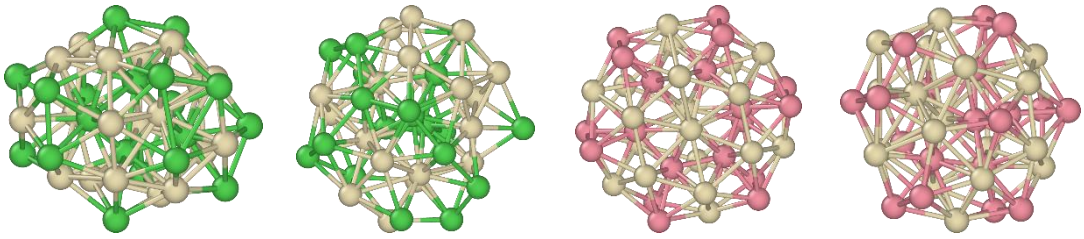

$Pt_{19}Ni_{19}$ (Str-1) $Pt_{19}Ni_{19}$ (Str-2) $Pt_{19}Co_{19}$ (Str-1) $Pt_{19}Co_{19}$ (Str-2)

Figure S2. Structural comparison of representative $Pt_{19}Ni_{19}$ and $Pt_{19}Co_{19}$ clusters optimized using Gupta potential (shown) and validated by DFT calculations. Left to right: $Pt_{19}Ni_{19}$ (Str-1), $Pt_{19}Ni_{19}$ (Str-2), $Pt_{19}Co_{19}$ (Str-1), $Pt_{19}Co_{19}$ (Str-2). Green/tan spheres represent Ni/Pt atoms; pink/tan spheres represent Co/Pt atoms.

Section S3: Optimized Cluster Structures

Figure S3. The optimized structures of (PtCo)38 clusters colored according to the atomic species

Co: red; Pt: blue

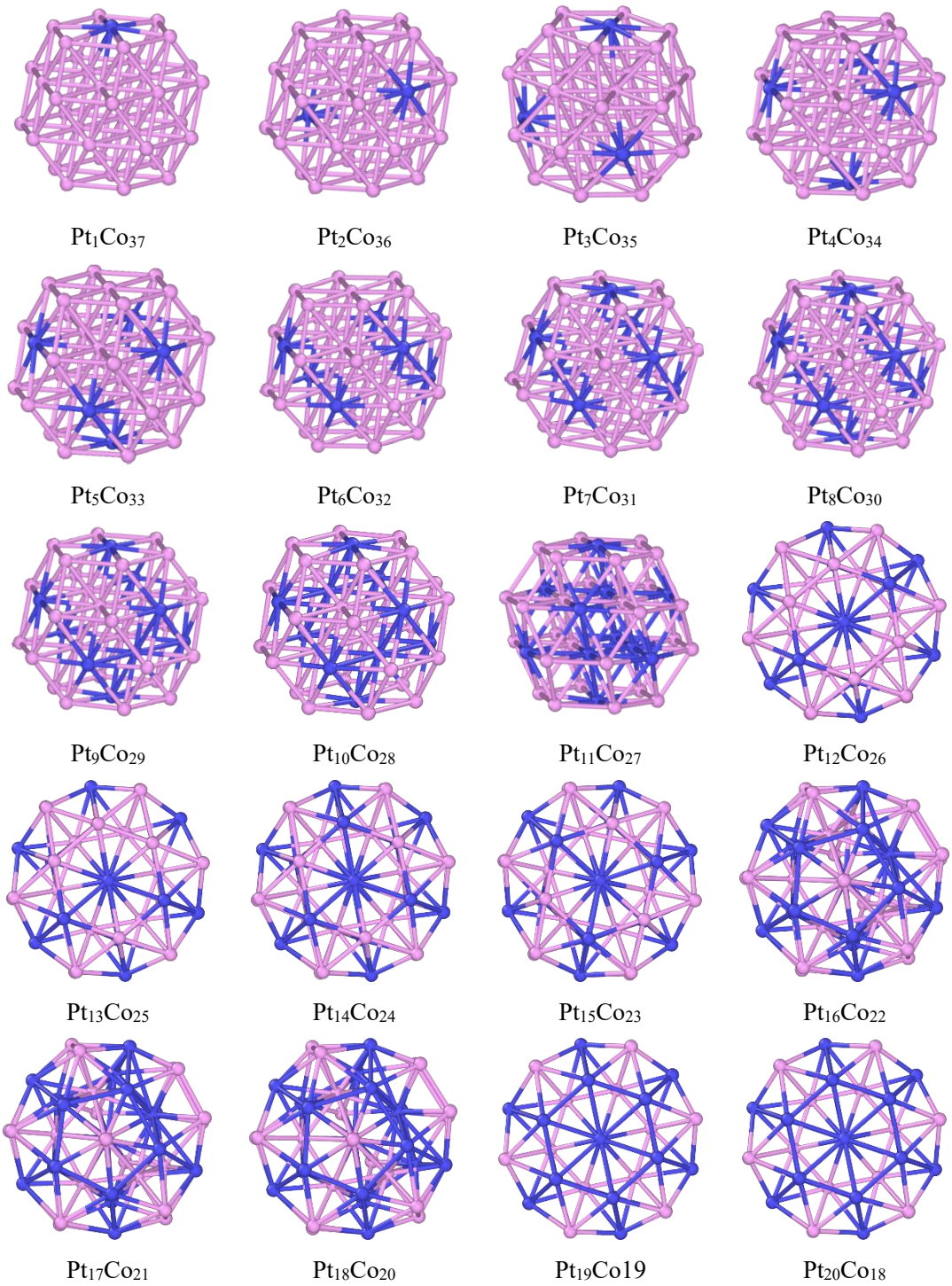

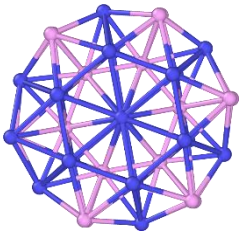

$Pt_{21}Co_{17}$

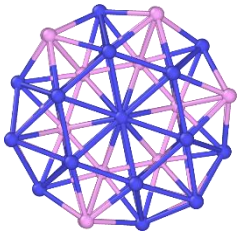

$Pt_{22}Co_{16}$

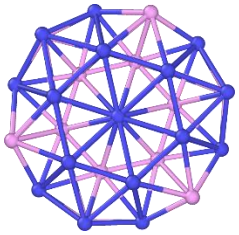

$Pt_{23}Co_{15}$

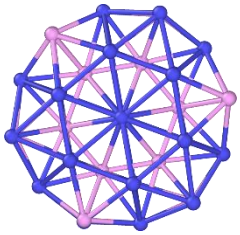

$Pt_{24}Co_{14}$

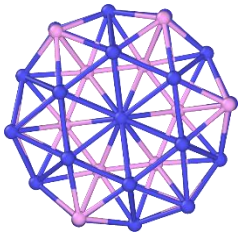

$Pt_{25}Co_{13}$

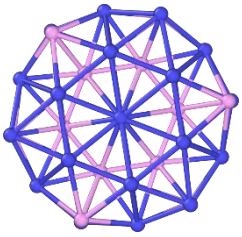

$Pt_{26}Co_{12}$

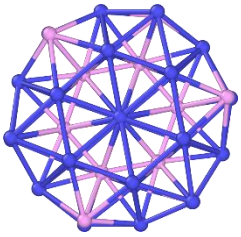

$Pt_{27}Co_{11}$

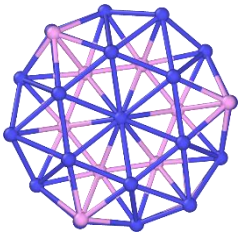

$Pt_{28}Co_{10}$

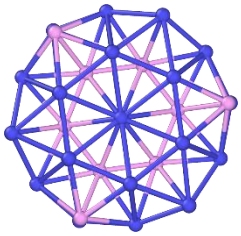

$Pt_{29}Co_{9}$

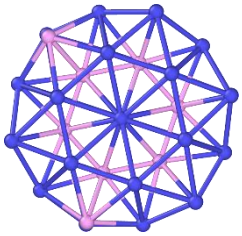

$Pt_{30}Co_{8}$

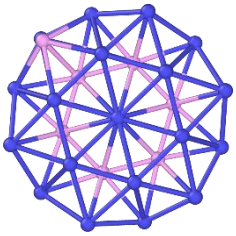

$Pt_{31}Co_{7}$

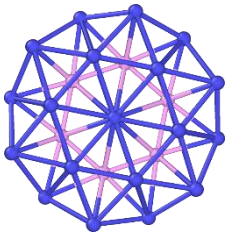

$Pt_{32}Co_{6}$

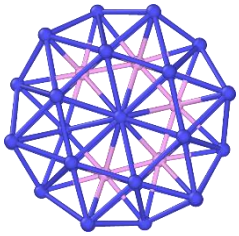

$Pt_{33}Co_{5}$

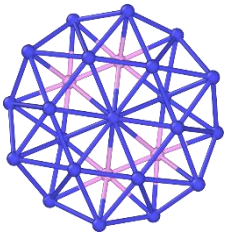

$Pt_{34}Co_{4}$

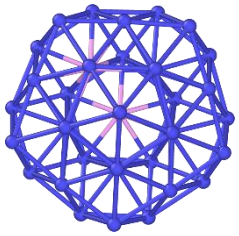

$Pt_{35}Co_{3}$

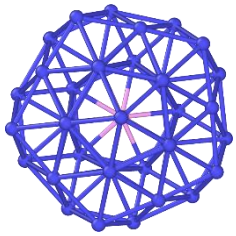

$Pt_{36}Co_{2}$

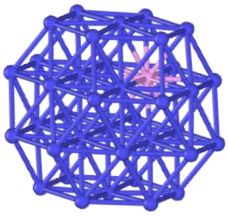

$Pt_{37}Co_{1}$

Figure S4. The optimized structures of (PtCo)38 clusters colored according to the atomic types

fcc: brown, icosahedral: yellow, others: white

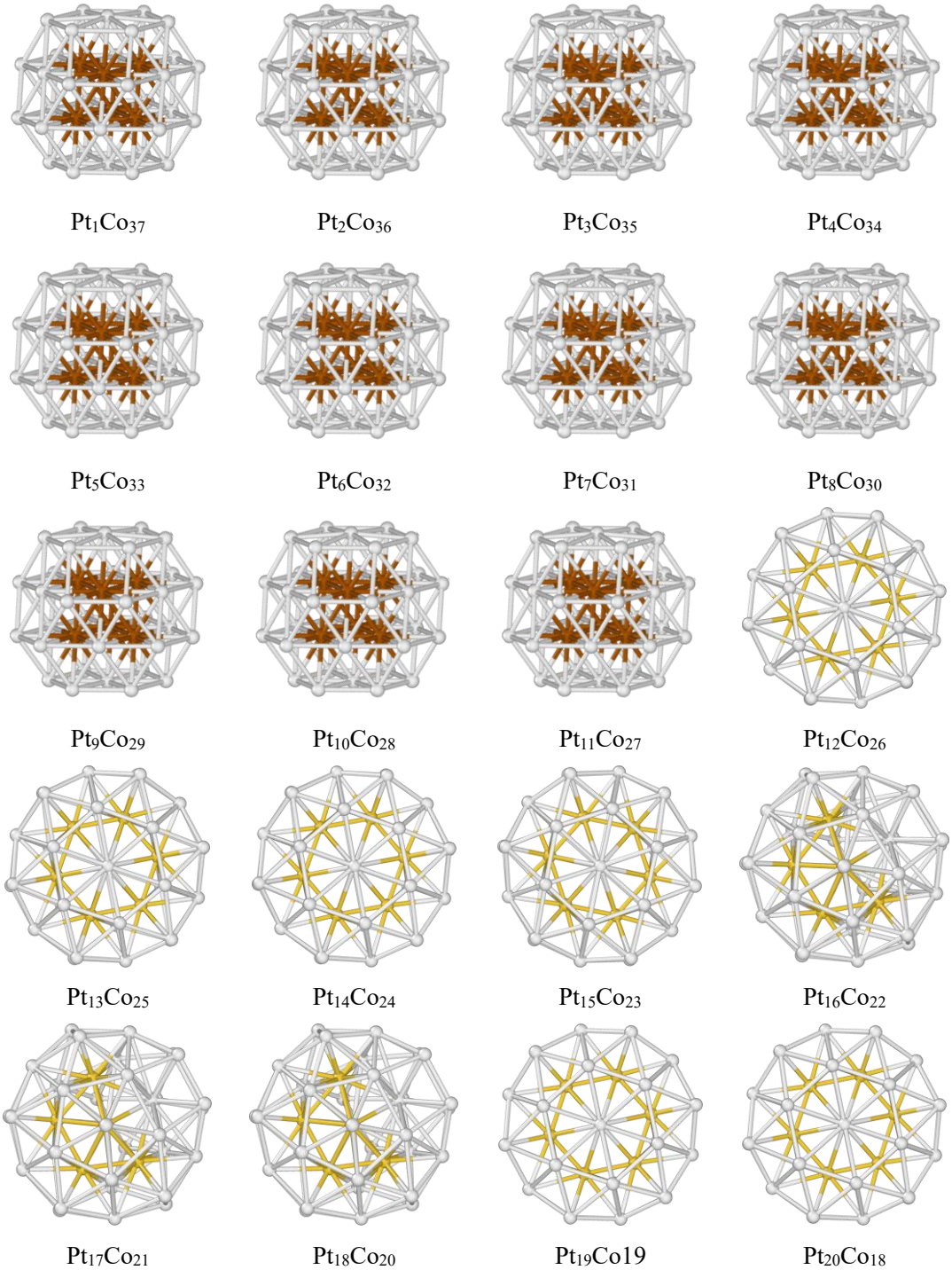

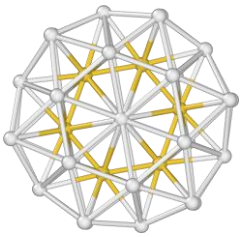

$Pt_{21}Co_{17}$

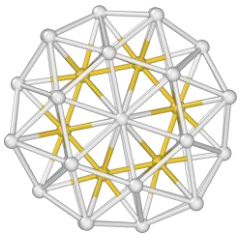

$Pt_{22}Co_{16}$

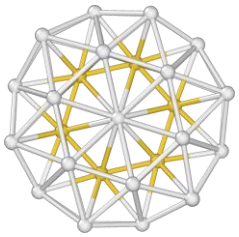

$Pt_{23}Co_{15}$

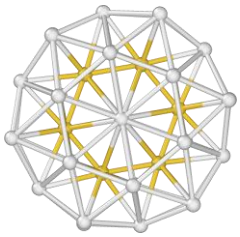

$Pt_{24}Co_{14}$

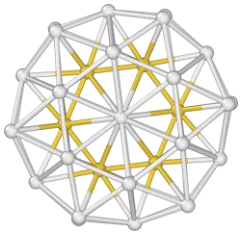

$Pt_{25}Co_{13}$

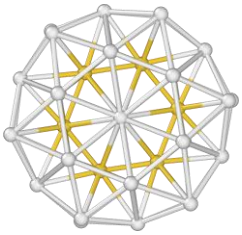

$Pt_{26}Co_{12}$

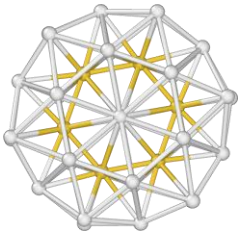

$Pt_{27}Co_{11}$

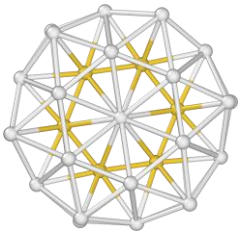

$Pt_{28}Co_{10}$

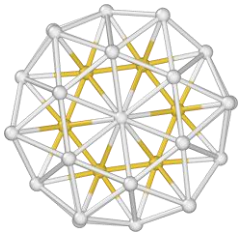

$Pt_{29}Co_{9}$

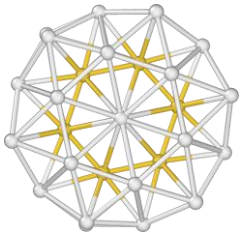

$Pt_{30}Co_{8}$

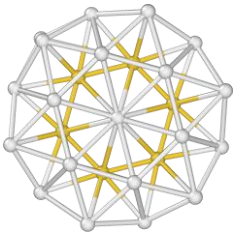

$Pt_{31}Co_{7}$

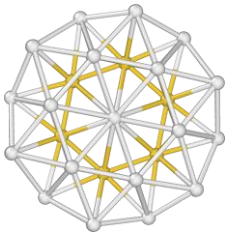

$Pt_{32}Co_{6}$

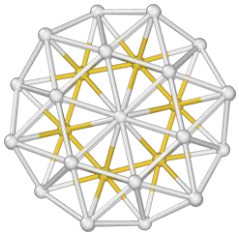

$Pt_{33}Co_{5}$

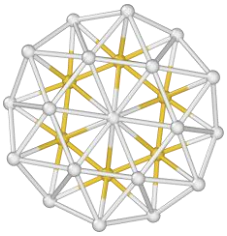

$Pt_{34}Co_{4}$

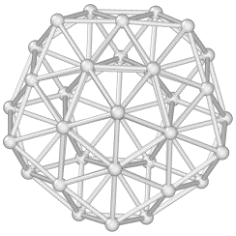

$Pt_{35}Co_{3}$

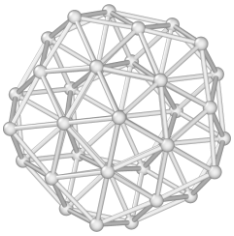

$Pt_{36}Co_{2}$

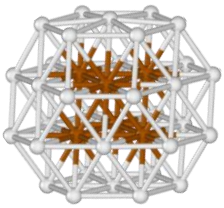

$Pt_{37}Co_{1}$

Figure S5. The optimized structures of (PtNi)38 clusters Nilored according to the atomic species

Pt: blue, Ni: green

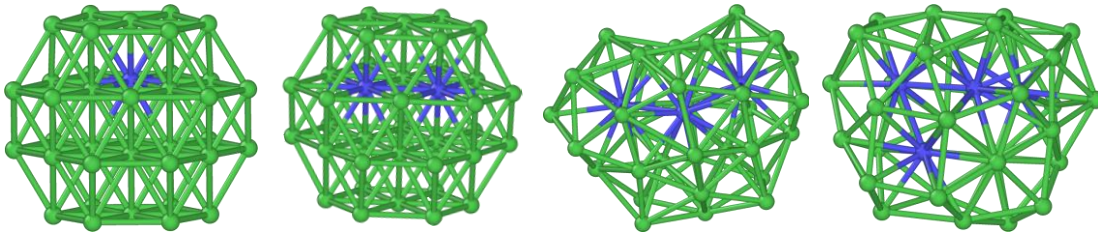

Pt_1Ni_{37} Pt_2Ni_{36} Pt_3Ni_{35} Pt_4Ni_{34}

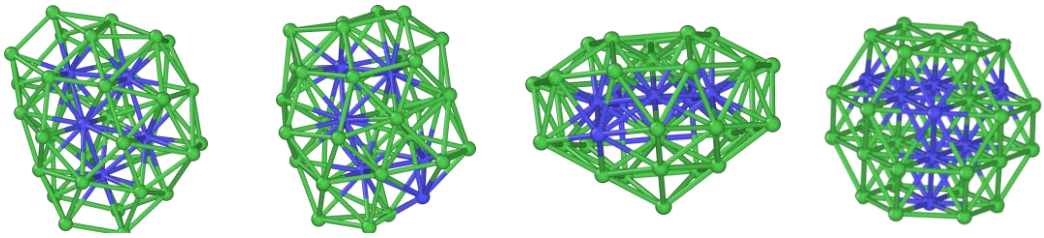

Pt_5Ni_{33} Pt_6Ni_{32} Pt_7Ni_{31} Pt_8Ni_{30}

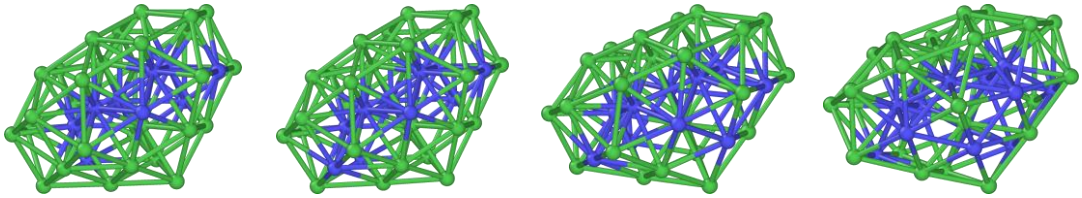

Pt_9Ni_{29} $Pt_{10}Ni_{28}$ $Pt_{11}Ni_{27}$ $Pt_{12}Ni_{26}$

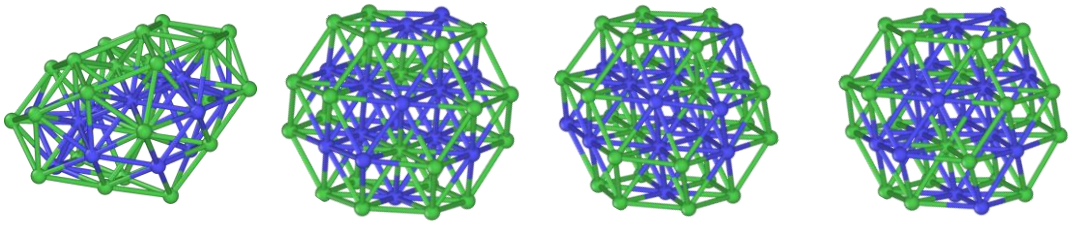

$Pt_{13}Ni_{25}$ $Pt_{14}Ni_{24}$ $Pt_{15}Ni_{23}$ $Pt_{16}Ni_{22}$

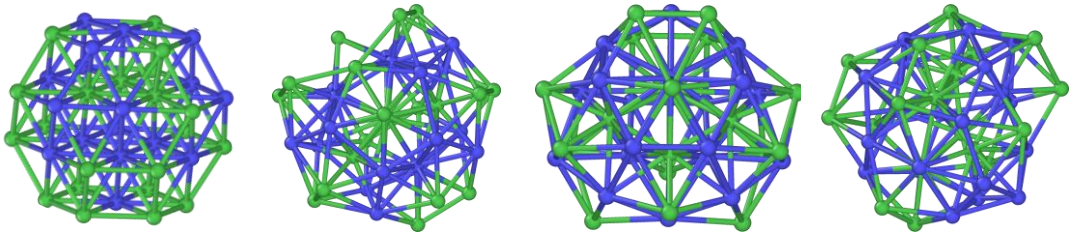

$Pt_{17}Ni_{21}$ $Pt_{18}Ni_{20}$ $Pt_{19}Ni19$ $Pt_{20}Ni_{18}$

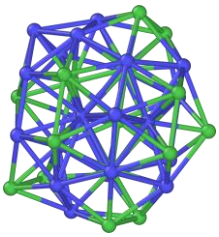

$Pt_{21}Ni_{17}$

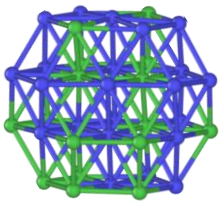

$Pt_{22}Ni_{16}$

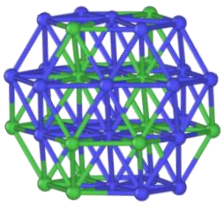

$Pt_{23}Ni_{15}$

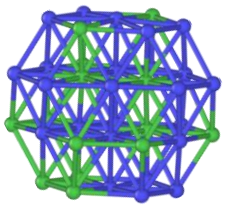

$Pt_{24}Ni_{14}$

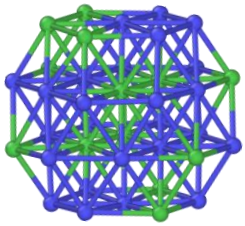

$Pt_{25}Ni_{13}$

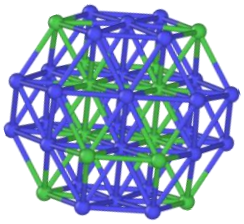

$Pt_{26}Ni_{12}$

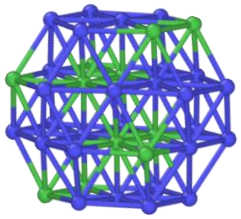

$Pt_{27}Ni_{11}$

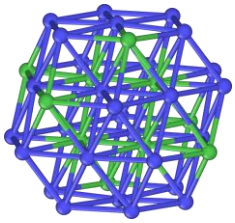

$Pt_{28}Ni_{10}$

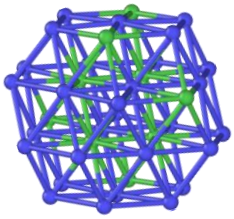

$Pt_{29}Ni_{9}$

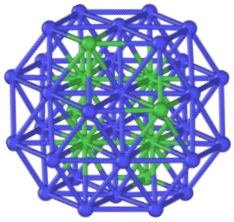

$Pt_{30}Ni_{8}$

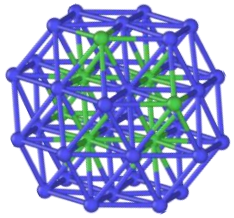

$Pt_{31}Ni_{7}$

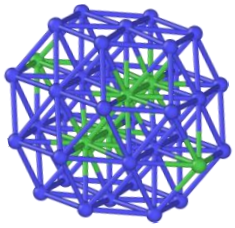

$Pt_{32}Ni_{6}$

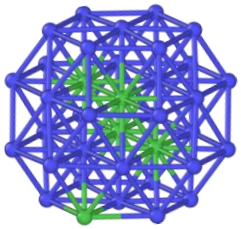

$Pt_{33}Ni_{5}$

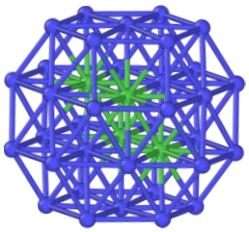

$Pt_{34}Ni_{4}$

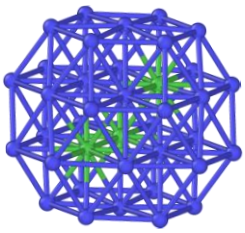

$Pt_{35}Ni_{3}$

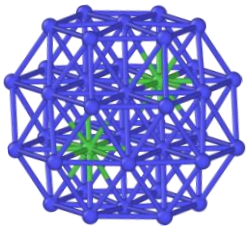

$Pt_{36}Ni_{2}$

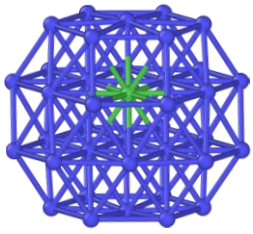

$Pt_{37}Ni_{1}$

Figure S6. The optimized structures of (PtNi)38 clusters Nilored according to the atomic types

fcc: brown, iNisahedral: yellow, others: white

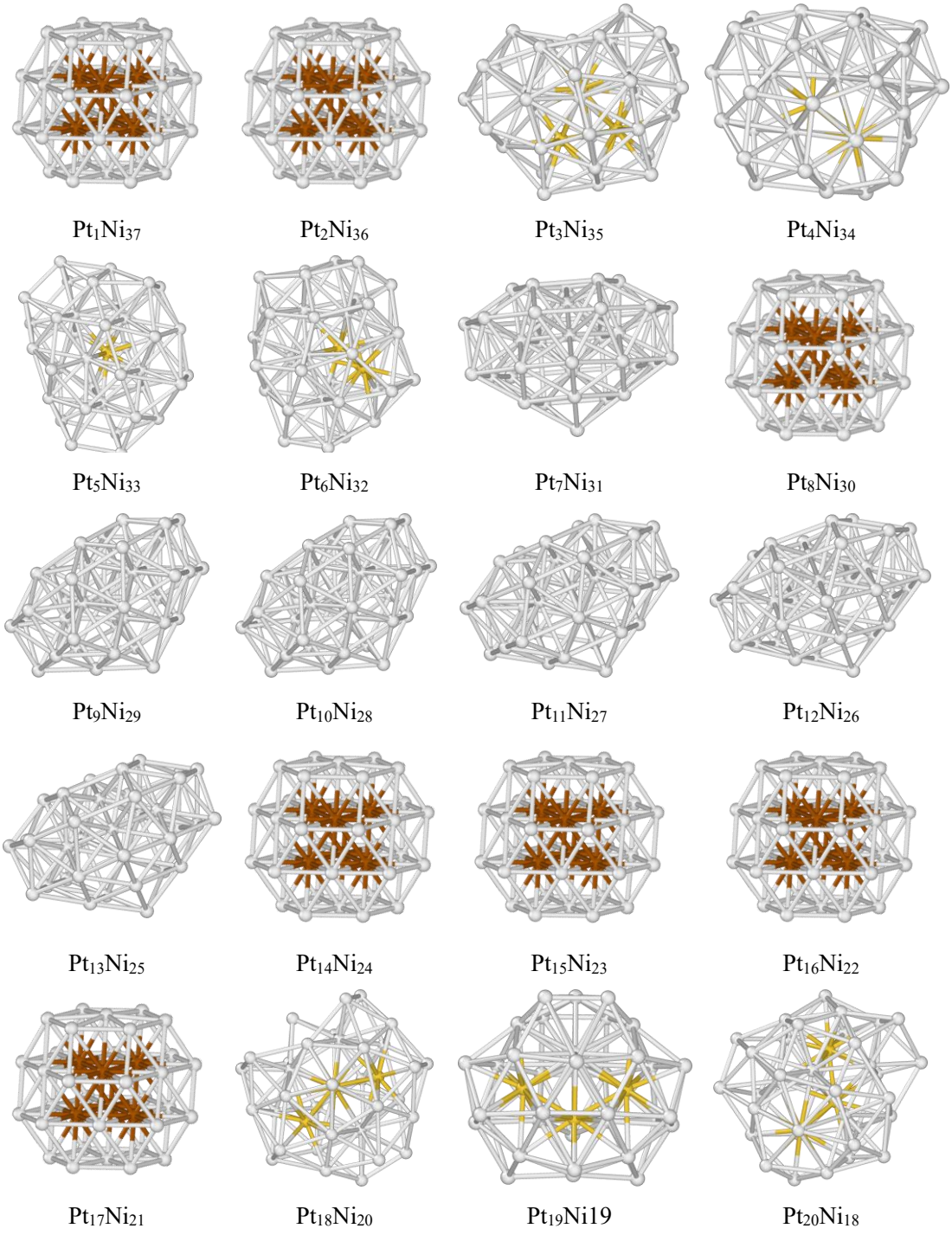

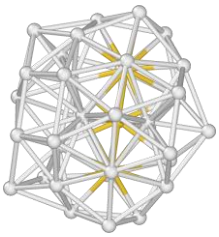

$Pt_{21}Ni_{17}$

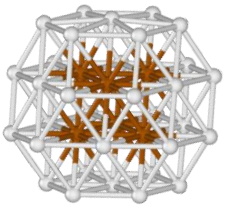

$Pt_{22}Ni_{16}$

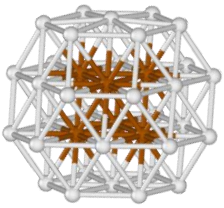

$Pt_{23}Ni_{15}$

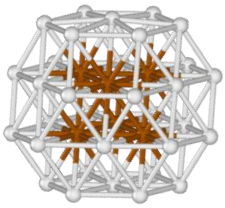

$Pt_{24}Ni_{14}$

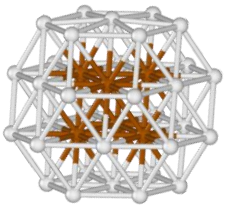

$Pt_{25}Ni_{13}$

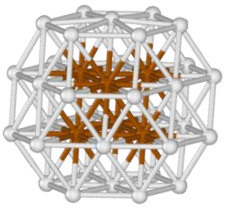

$Pt_{26}Ni_{12}$

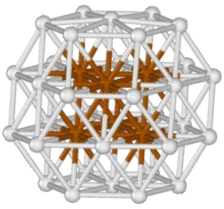

$Pt_{27}Ni_{11}$

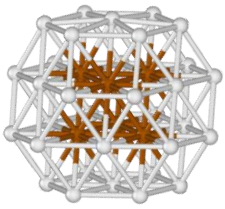

$Pt_{28}Ni_{10}$

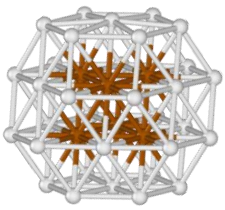

$Pt_{29}Ni_{9}$

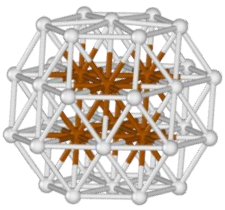

$Pt_{30}Ni_{8}$

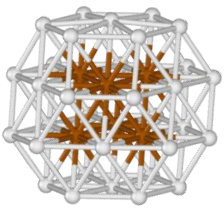

$Pt_{31}Ni_{7}$

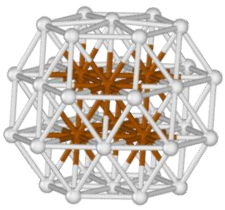

$Pt_{32}Ni_{6}$

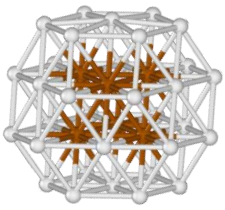

$Pt_{33}Ni_{5}$

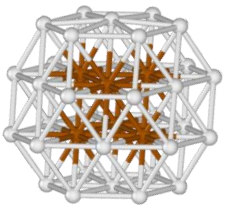

$Pt_{34}Ni_{4}$

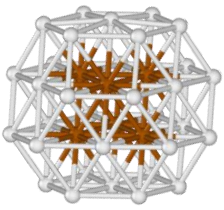

$Pt_{35}Ni_{3}$

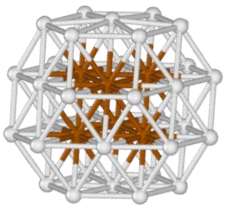

$Pt_{36}Ni_{2}$

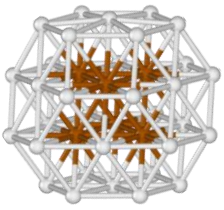

$Pt_{37}Ni_{1}$

Figure S7. The optimized structures of (PtCo)55 clusters colored according to the atomic species

Co: red; Pt: blue

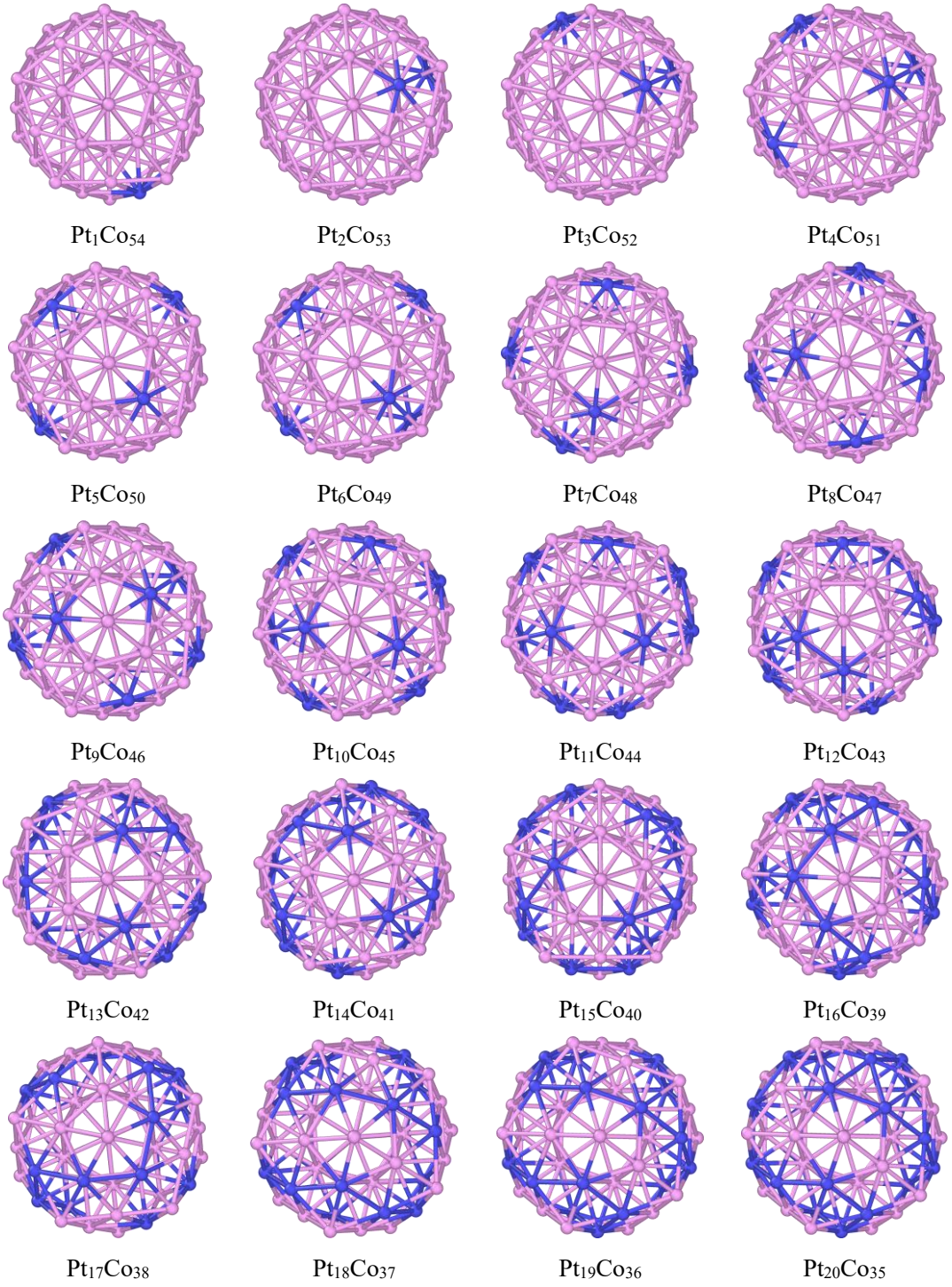

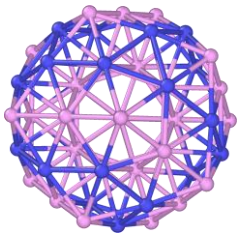

$Pt_{21}Co_{34}$

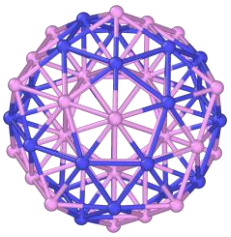

$Pt_{22}Co_{33}$

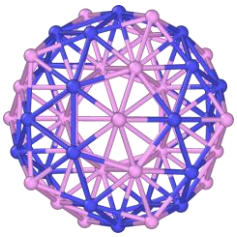

$Pt_{23}Co_{32}$

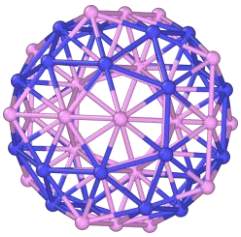

$Pt_{24}Co_{31}$

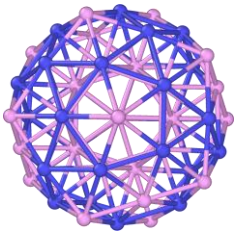

$Pt_{25}Co_{30}$

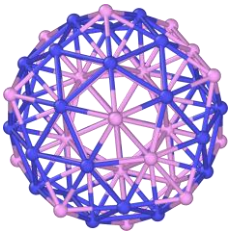

$Pt_{26}Co_{29}$

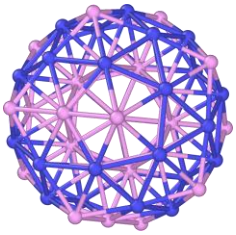

$Pt_{27}Co_{28}$

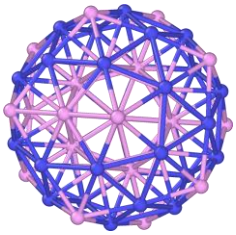

$Pt_{28}Co_{27}$

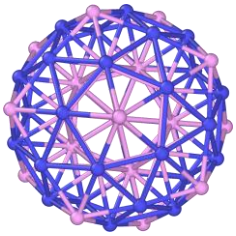

$Pt_{29}Co_{26}$

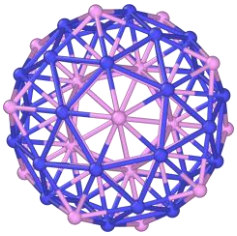

$Pt_{30}Co_{25}$

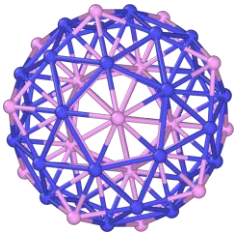

$Pt_{31}Co_{24}$

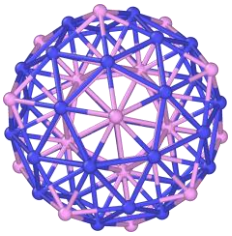

$Pt_{32}Co_{23}$

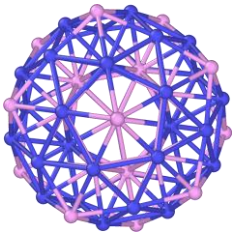

$Pt_{33}Co_{22}$

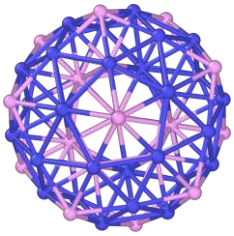

$Pt_{34}Co_{21}$

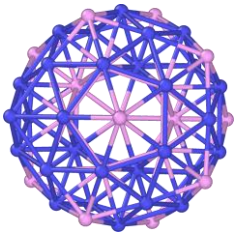

$Pt_{35}Co_{20}$

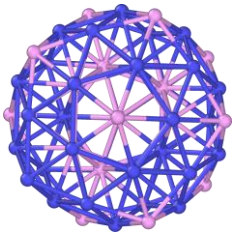

$Pt_{36}Co_{19}$

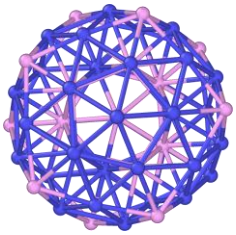

$Pt_{37}Co_{18}$

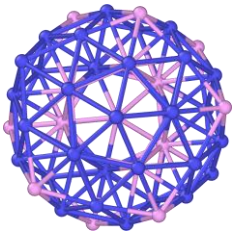

$Pt_{38}Co_{17}$

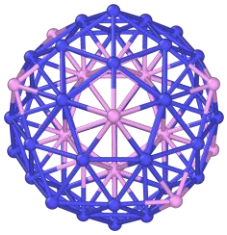

$Pt_{39}Co_{16}$

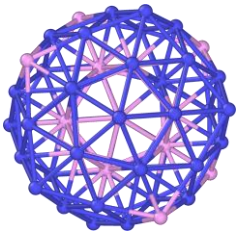

$Pt_{40}Co_{15}$

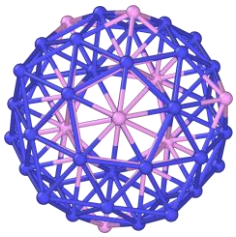

$Pt_{41}Co_{14}$

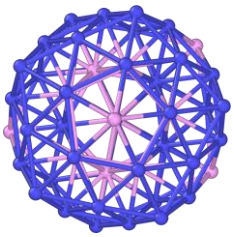

$Pt_{42}Co_{13}$

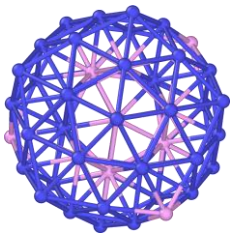

$Pt_{43}Co_{12}$

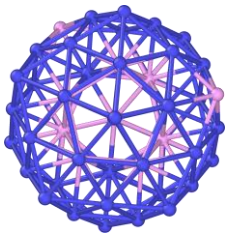

$Pt_{44}Co_{11}$

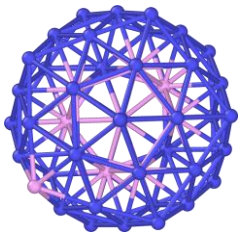

$Pt_{45}Co_{10}$

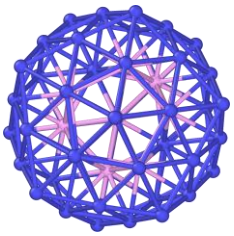

$Pt_{46}Co_{9}$

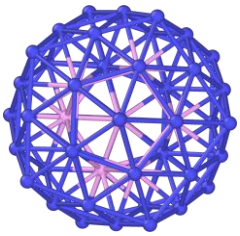

$Pt_{47}Co_{8}$

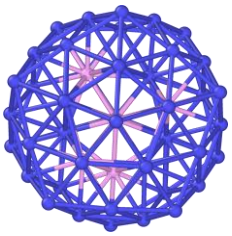

$Pt_{48}Co_{7}$

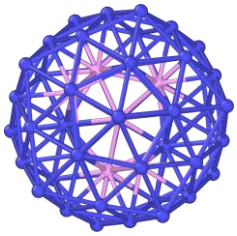

$Pt_{49}Co_{6}$

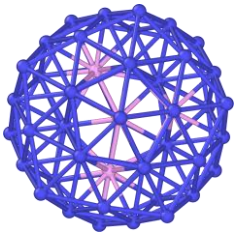

$Pt_{50}Co_{5}$

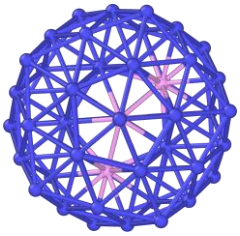

$Pt_{51}Co_{4}$

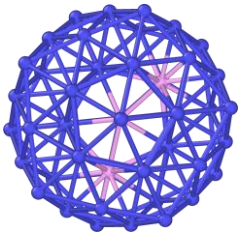

$Pt_{52}Co_{3}$

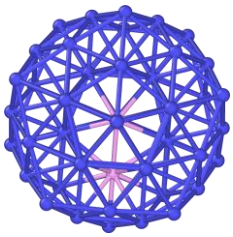

$Pt_{53}Co_{2}$

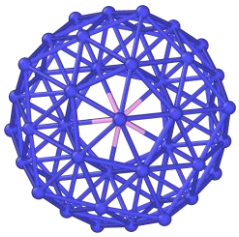

$Pt_{54}Co_{1}$

Figure S8. The optimized structures of (PtNi)55 clusters colored according to the atomic species

Pt: blue;, Ni: green

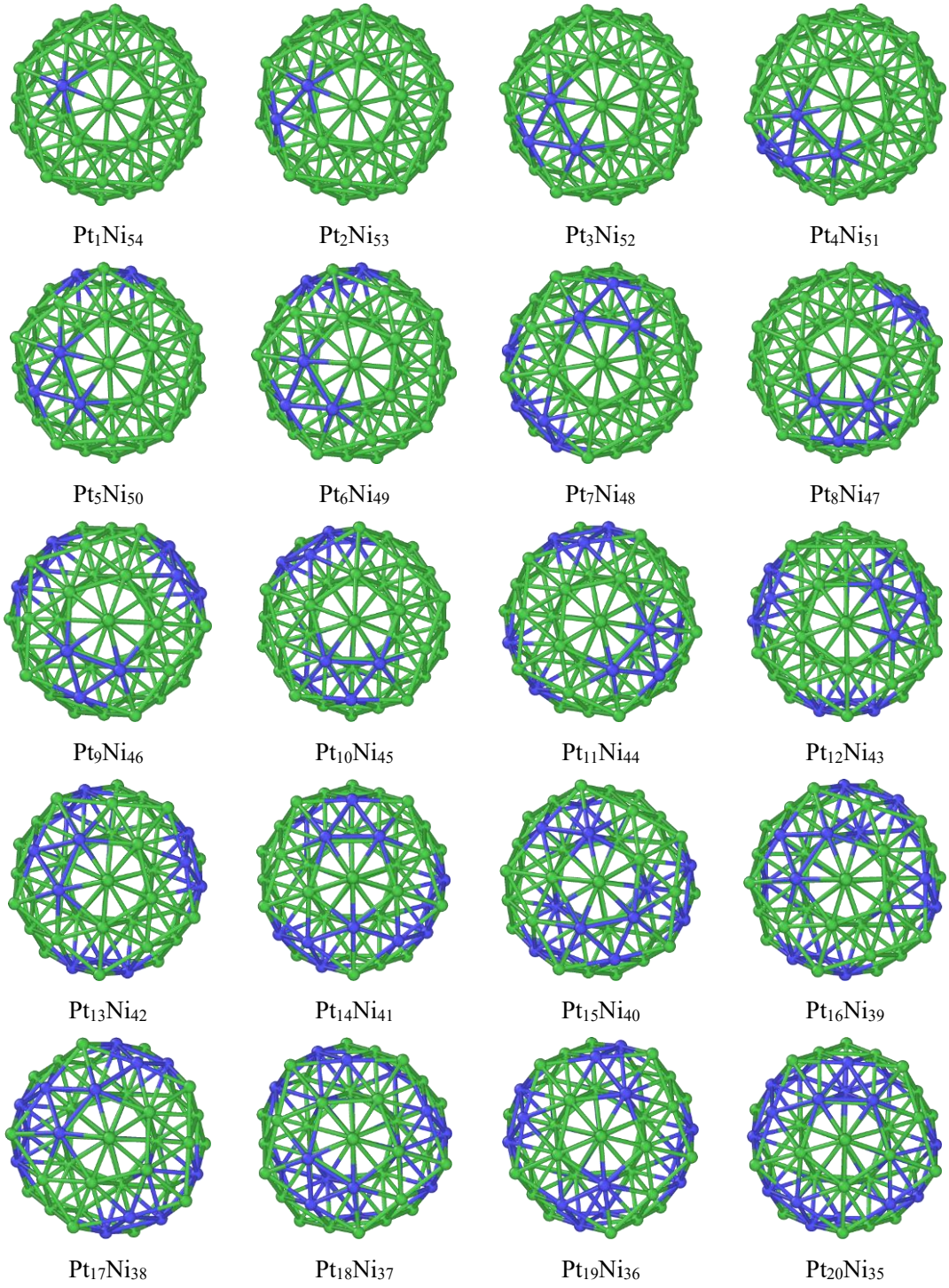

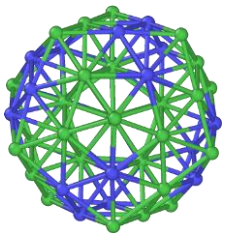

$Pt_{21}Ni_{34}$

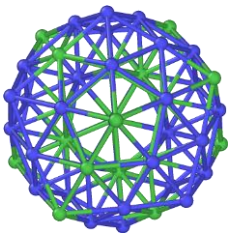

$Pt_{22}Ni_{33}$

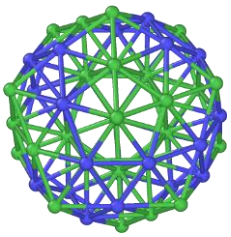

$Pt_{23}Ni_{32}$

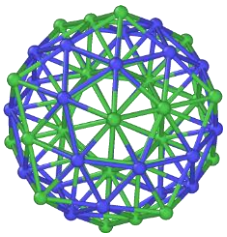

$Pt_{24}Ni_{31}$

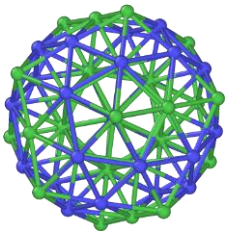

$Pt_{25}Ni_{30}$

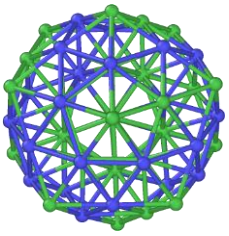

$Pt_{26}Ni_{29}$

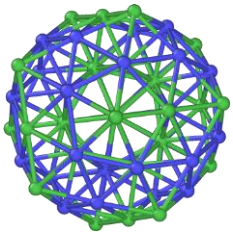

$Pt_{27}Ni_{28}$

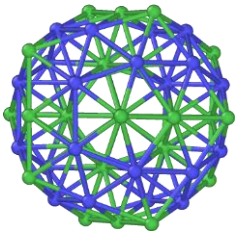

$Pt_{28}Ni_{27}$

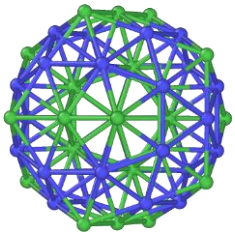

$Pt_{29}Ni_{26}$

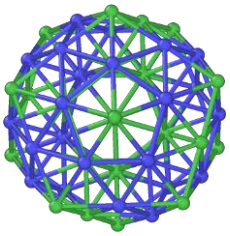

$Pt_{30}Ni_{25}$

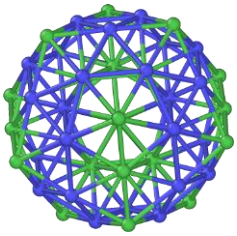

$Pt_{31}Ni_{24}$

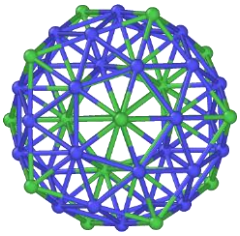

$Pt_{32}Ni_{23}$

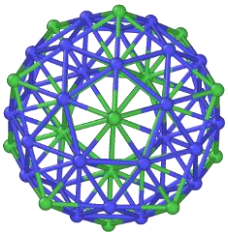

$Pt_{33}Ni_{22}$

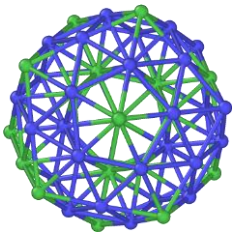

$Pt_{34}Ni_{21}$

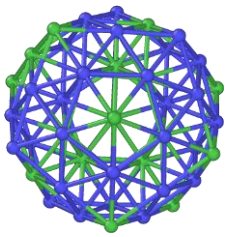

$Pt_{35}Ni_{20}$

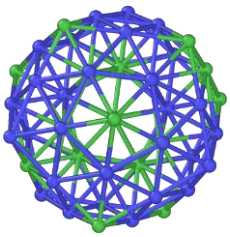

$Pt_{36}Ni_{19}$

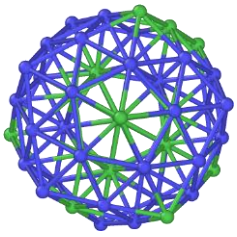

$Pt_{37}Ni_{18}$

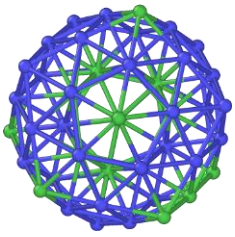

$Pt_{38}Ni_{17}$

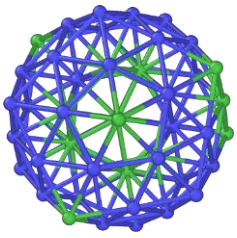

$Pt_{39}Ni_{16}$

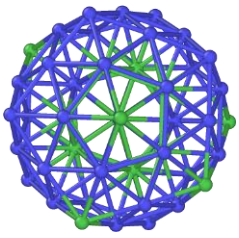

$Pt_{40}Ni_{15}$

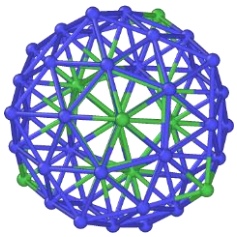

$Pt_{41}Ni_{14}$

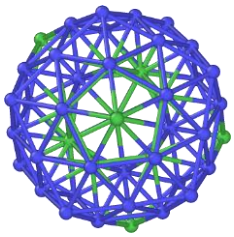

$Pt_{42}Ni_{13}$

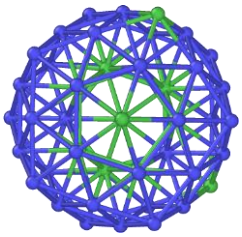

$Pt_{43}Ni_{12}$

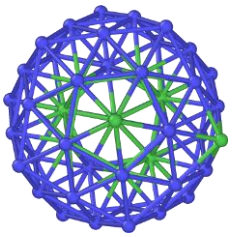

$Pt_{44}Ni_{11}$

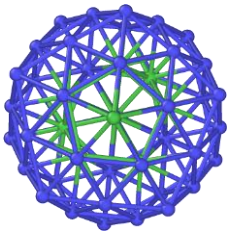

$Pt_{45}Ni_{10}$

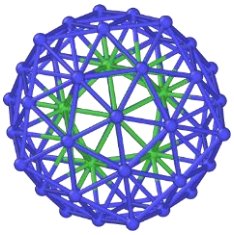

$Pt_{46}Ni_{9}$

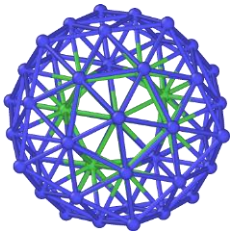

$Pt_{47}Ni_{8}$

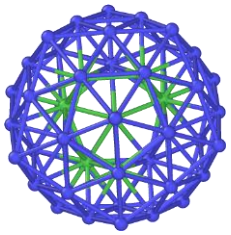

$Pt_{48}Ni_{7}$

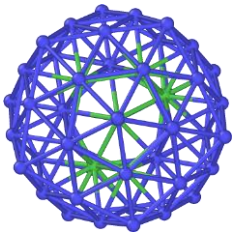

$Pt_{49}Ni_{6}$

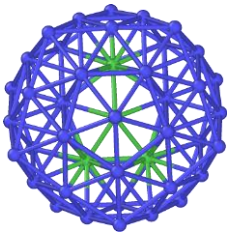

$Pt_{50}Ni_{5}$

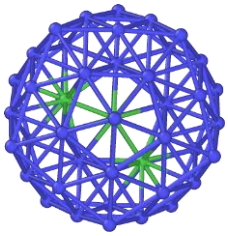

$Pt_{51}Ni_{4}$

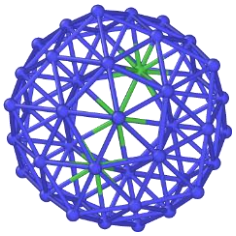

$Pt_{52}Ni_{3}$

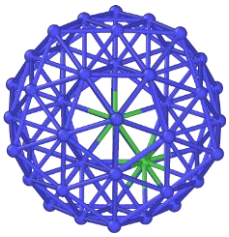

$Pt_{53}Ni_{2}$

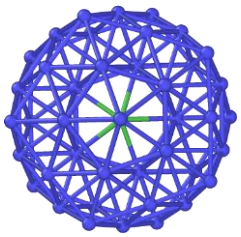

$Pt_{54}Ni_{1}$

Section S4: Bond Length and Structural Similarity Analysis

Figure S9. Mean bond length as a function of Ni fraction for N=55 clusters.

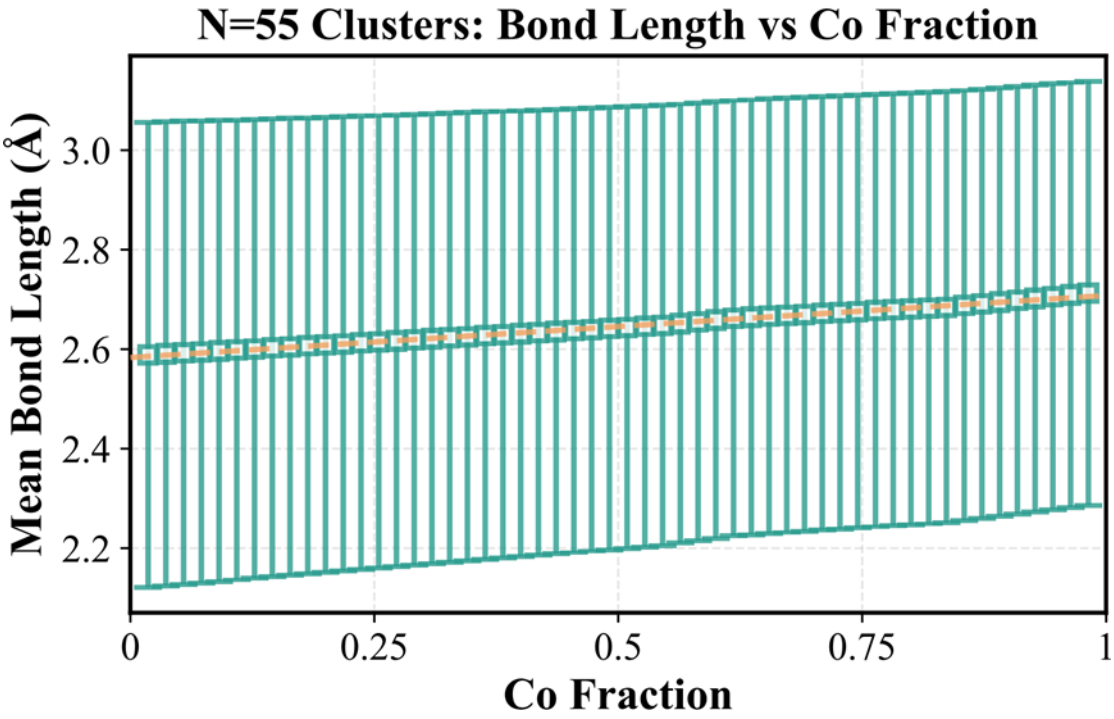

Figure S10. The similarity analysis results of PtNi clusters to Ni reference.

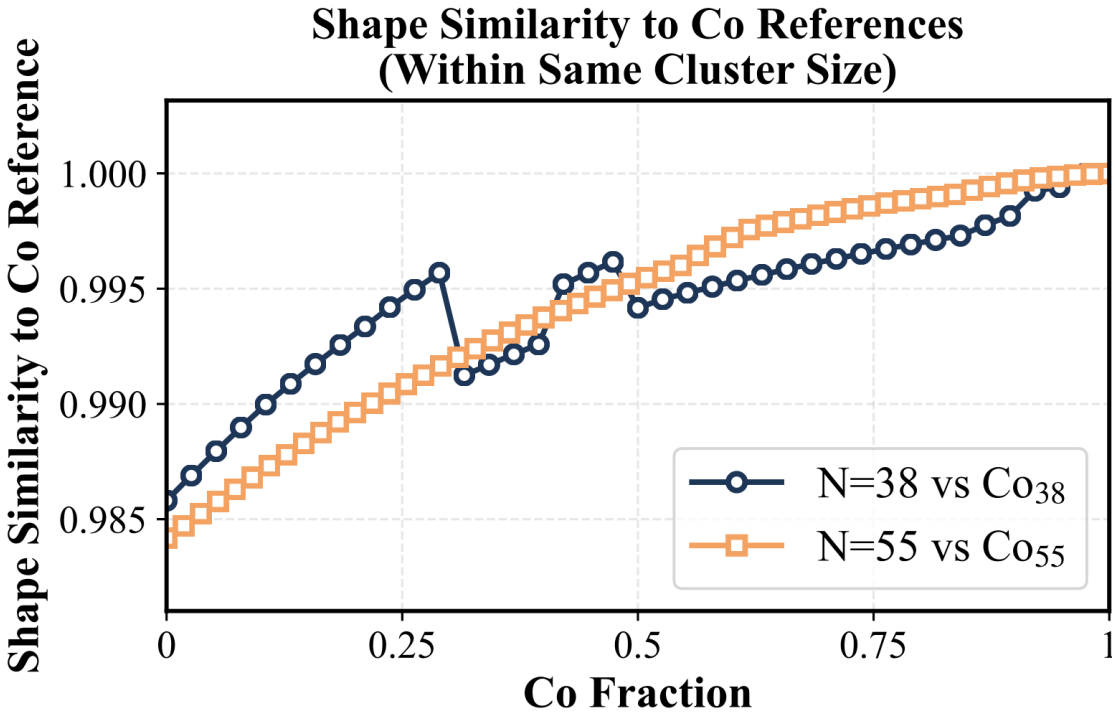

Figure S11. Mean bond length as a function of Ni fraction for N=55 clusters.

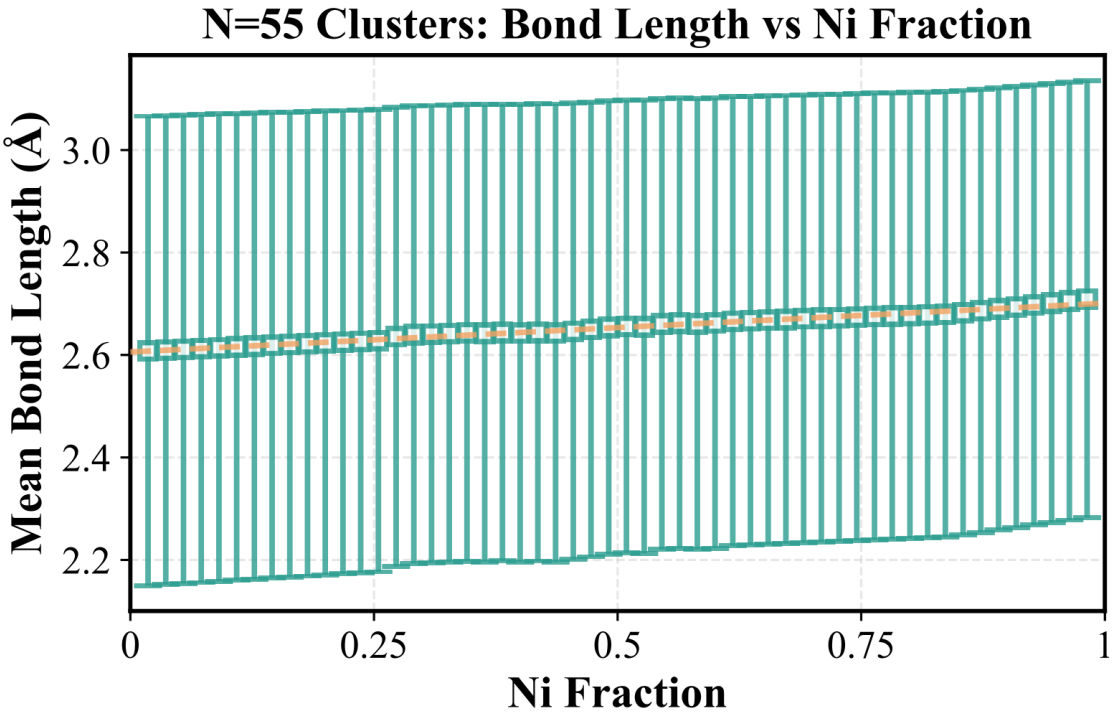

Figure S12. The similarity analysis results of PtNi clusters to Ni reference.

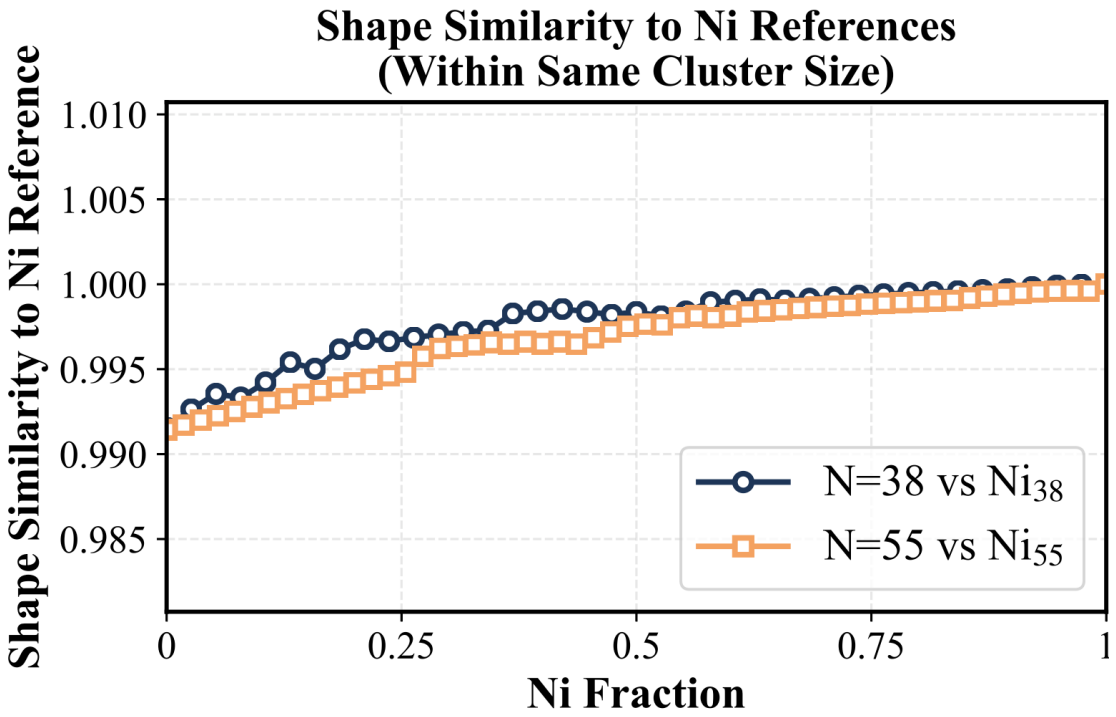

Section S5: Electronic Structure Analysis

we have performed comprehensive density functional theory (DFT) calculations including spin-polarized density of states (DOS), projected density of states (PDOS) on d-orbitals, and quantitative d-band center analysis. These additional calculations and analyses have been incorporated into the revised manuscript and provide crucial insights into the electronic origins of the observed catalytic behavior differences.

The electronic structure analysis reveals fundamental differences between PtCo and PtNi systems that provide microscopic insight into their distinct structural and catalytic behaviors. The magnetic properties show the most striking contrast between the two systems. $Pt_{19}Co_{19}$ exhibits strong ferromagnetic behavior with pronounced spin polarization visible in both Pt and Co d-orbitals. Both elements show significant separation between spin-up (positive) and spin-down (negative) states, indicating substantial local magnetic moments throughout the cluster. The total DOS (Figure S13) displays large spin splitting throughout the occupied states, with spin-up and spin-down channels clearly separated across the entire energy range. In contrast, $Pt_{19}Ni_{19}$ shows much weaker magnetic character. While Ni retains some spin polarization with spin-up states dominating, the spin-down contribution is minimal compared to the Co-containing system. Pt atoms in the PtNi environment show almost no spin polarization. The total DOS (Figure S14) confirms this weak magnetic nature, with spin-up states dominating and very weak spin-down contributions. This fundamental difference in magnetic behavior has important implications for catalytic applications, as magnetic properties can influence adsorption energies and reaction pathways.

The d-orbital characteristics provide further insight into the electronic distinctions between these systems. In $Pt_{19}Co_{19}$ (Figure S15), Pt d-orbitals show a broad distribution with multiple peaks between -8 eV and the Fermi level, with significant contributions from both spin-up and spin-down states. The presence of substantial spin-down states (shown as negative values in the PDOS plots) indicates strong magnetic coupling with Co atoms. Co d-orbitals exhibit a broad distribution centered around -5 to -4 eV below the Fermi level, with very strong spin polarization. The spin-up states show peak intensities around 27 states/eV, while spin-down states show even larger negative values reaching -33 states/eV, characteristic of Co's ferromagnetic nature. The broad distribution of Co d-states and their significant overlap with Pt d-orbitals suggest strong d-d hybridization between the two elements, which influences both structural preferences and reactivity.

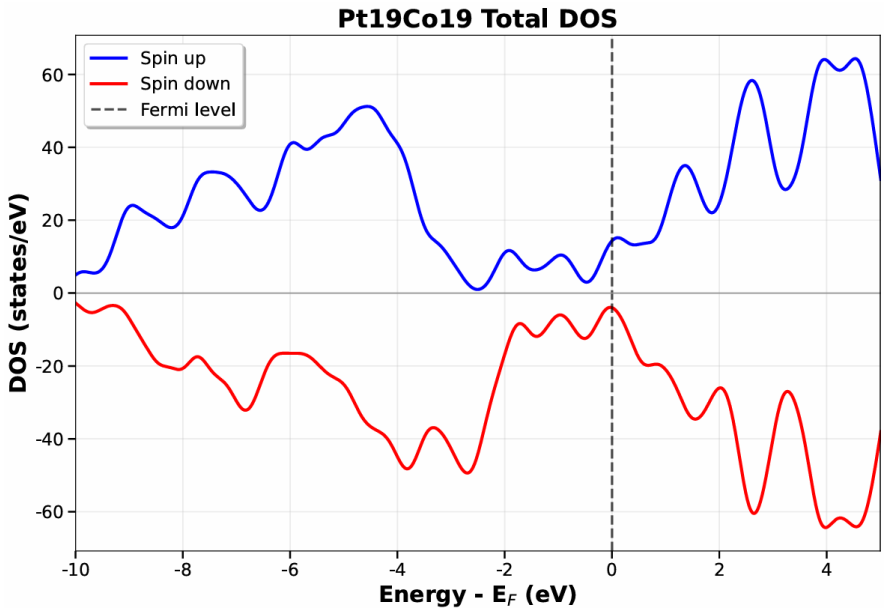

Figure S13. Total DOS for $Pt_{19}Co_{19}$ cluster

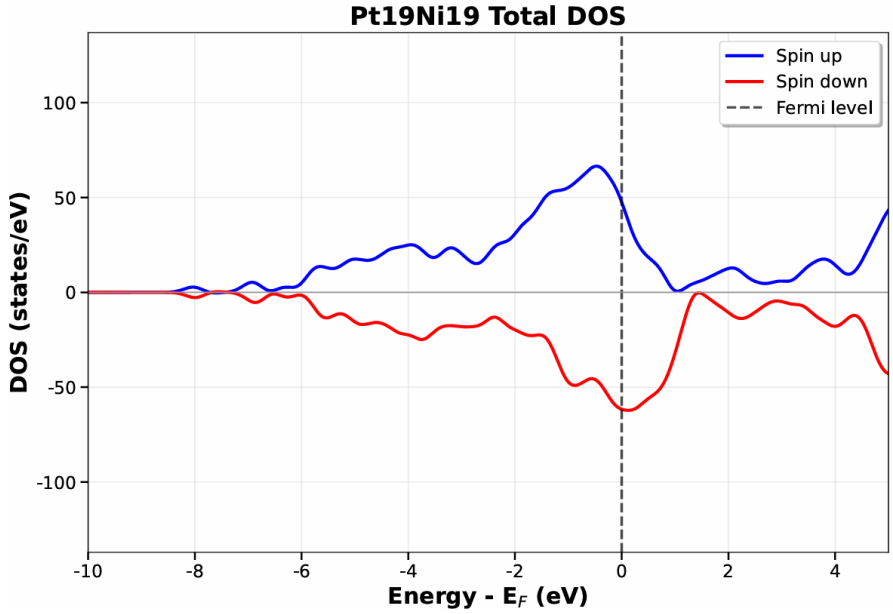

Figure S14. Total DOS for $Pt_{19}Ni_{19}$ cluster

In $Pt_{19}Ni_{19}$ (Figure S16), Pt d-orbitals display a characteristic two-peak structure with peaks around -4 eV and -1 eV below the Fermi level, predominantly in the spin-up channel. The near absence of spin-down states indicates weak magnetic polarization in the PtNi environment, contrasting sharply with the behavior in PtCo. Ni d-orbitals show a sharp, intense peak centered very close to the Fermi level (approximately -0.5 to -1.0 eV below EF), with peak intensity reaching approximately 40 states/eV in the spin-up channel. This high density of states near the Fermi level is characteristic of Ni and plays a crucial role in determining chemical reactivity and catalytic properties. The spin-down contribution is minimal, confirming weak magnetic polarization. The sharp localization of Ni d-states near the Fermi level, in contrast to the broader distribution of Co d-states, suggests different bonding characteristics and reactivity patterns between the two alloy systems.

The d-band center (εd), calculated as the first moment of the d-PDOS weighted by occupation,

provides important insights into catalytic activity. Ni exhibits a d-band center located very close to the Fermi level (approximately -0.7 eV), suggesting strong binding interactions with adsorbates. Co shows its d-band center positioned further from the Fermi level (approximately -2.0 to -2.5 eV), indicating intermediate binding strength. Pt exhibits intermediate d-band positions in both systems but is shifted by interaction with Co or Ni. According to the d-band model, systems with d-band centers closer to the Fermi level typically exhibit stronger adsorption energies. This suggests that PtNi clusters may show higher catalytic activity for reactions requiring strong adsorbate binding, such as oxygen reduction reaction, while PtCo clusters with their magnetic properties and intermediate d-band positions may be favorable for reactions benefiting from spin-polarized electronic states.

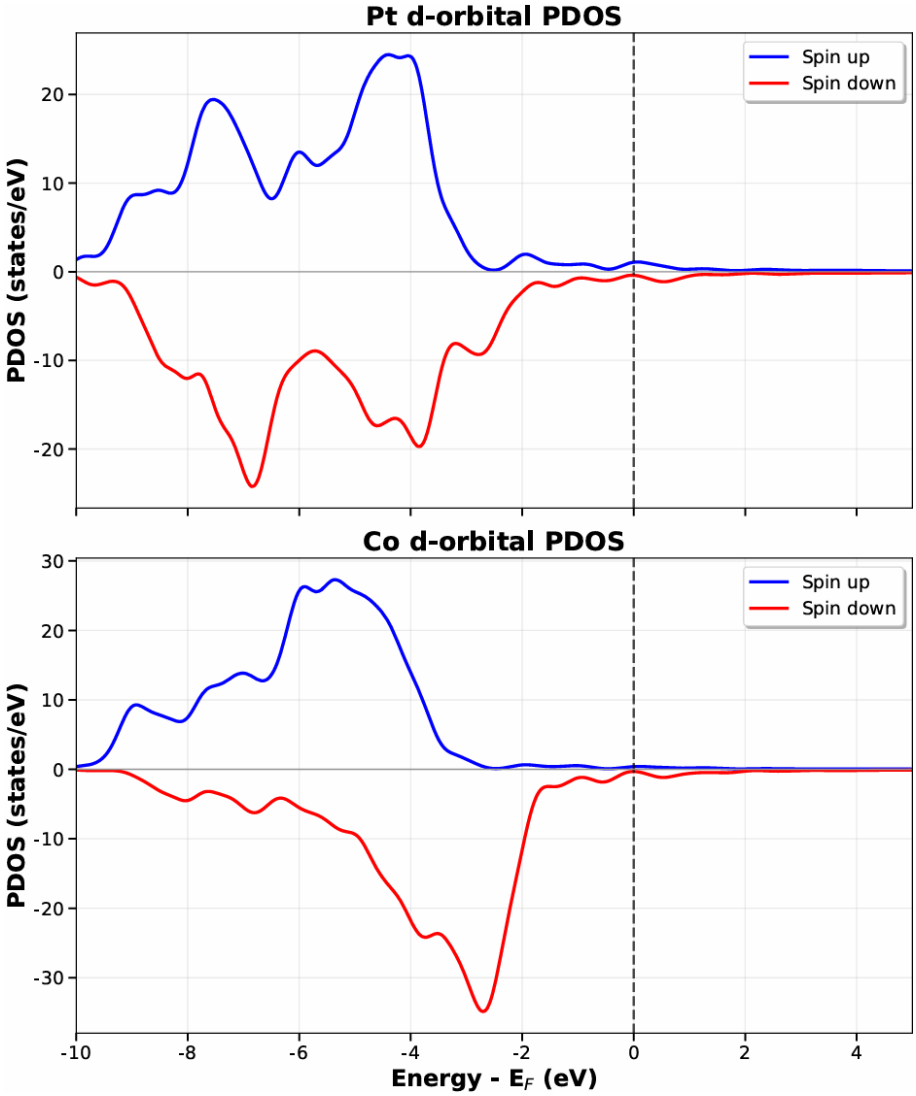

Figure S15. d-orbital PDOS for Pt and Co in $Pt_{19}Co_{19}$ cluster

The total DOS provides an integrated view of how these atomic-level electronic features combine to determine overall electronic structure. $Pt_{19}Co_{19}$ (Figure S13) shows a complex multi-peak structure throughout the occupied states with strong spin splitting. The occupied states extend significantly below the Fermi level with multiple features in both spin channels, reflecting strong d-d hybridization between Pt and Co. The magnetic character dominates the entire electronic structure, with substantial separation between spin-up and spin-down states across the full energy range.

$Pt_{19}Ni_{19}$ (Figure S16) exhibits a prominent sharp peak just below the Fermi level around -1 eV, dominated by Ni d-states, with much weaker magnetic character. The electronic states near the Fermi level are crucial for chemical reactivity and catalytic performance, and the sharp Ni-derived peak suggests high electronic availability for bonding with adsorbates.

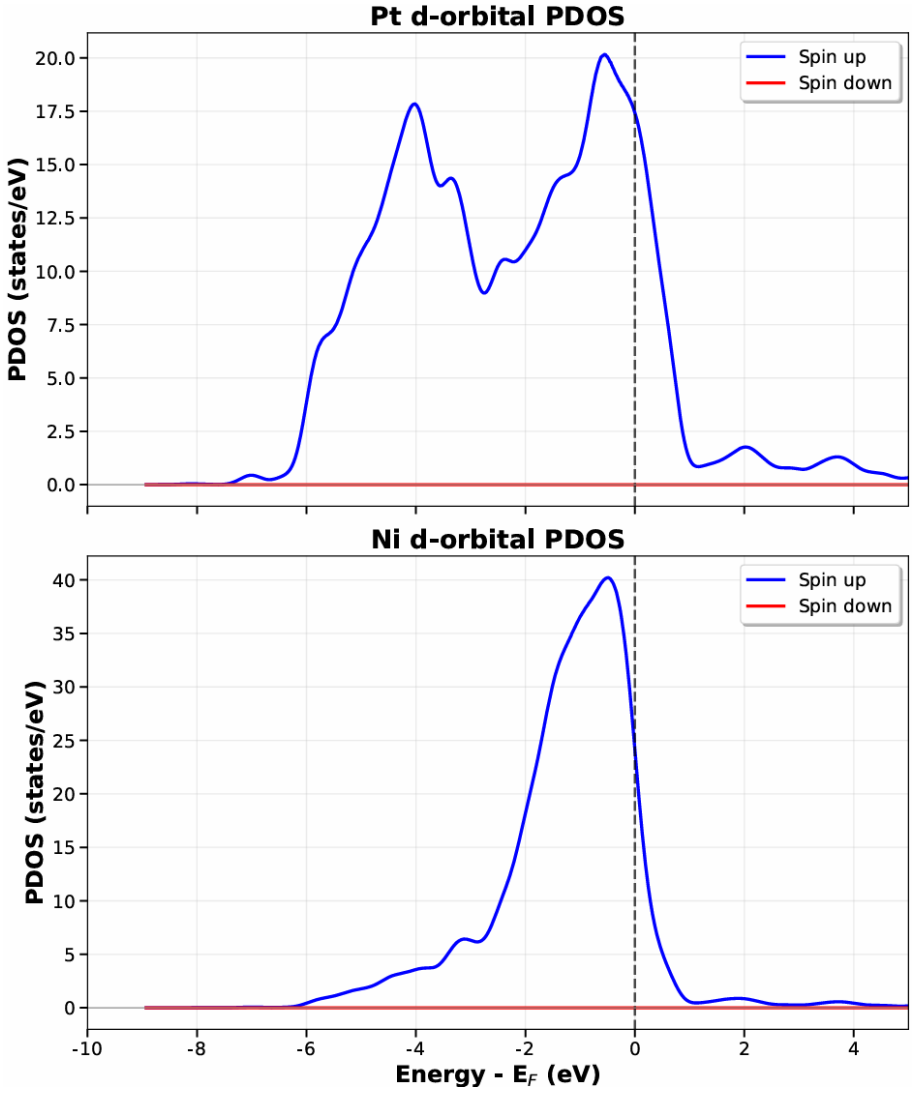

Figure S16. d-orbital PDOS for Pt and Ni in $Pt_{19}Ni_{19}$ cluster

These electronic structure differences correlate well with the structural preferences observed in the main manuscript. PtCo's strong magnetic coupling and broader d-state distribution may favor the mixed structural motifs observed in the structural analysis, as magnetic interactions can influence atomic arrangement preferences. The strong magnetic moments and spin polarization in PtCo systems provide an additional interaction mechanism beyond purely geometric considerations, potentially explaining the complex excess energy profiles and preference for specific core-shell arrangements. PtNi's sharp d-band peak near the Fermi level and weak magnetism correlate with its tendency toward clearer segregation patterns and more stable core-shell structures. The electronic structure suggests that PtNi systems are primarily governed by geometric and size mismatch effects rather than magnetic considerations, leading to the more systematic structural trends observed in bond length and BOP analyses. The different degrees of d-d orbital hybridization between Pt-Co and Pt-Ni explain the distinct excess energy profiles and structural preferences observed in the

systematic compositional studies.

The electronic structure analysis reveals that PtCo and PtNi bimetallic clusters possess fundamentally different electronic and magnetic properties that underlie their distinct structural and catalytic behaviors. PtCo systems exhibit strong ferromagnetism with pronounced spin polarization and broadly distributed d-states, while PtNi systems show weak magnetic character with d-states sharply peaked near the Fermi level. These electronic distinctions provide a microscopic basis for understanding the different structural preferences, segregation behaviors, and potential catalytic activities of the two alloy systems characterized in the main manuscript. The strong magnetic coupling in PtCo versus the high Fermi-level d-state density in PtNi explains why these structurally similar systems exhibit such different mixing behaviors, excess energy profiles, and structural evolution patterns. This electronic-level understanding validates that the comparative structural analysis presented in the main manuscript reflects genuine physical differences between the two alloy families rather than computational artifacts.